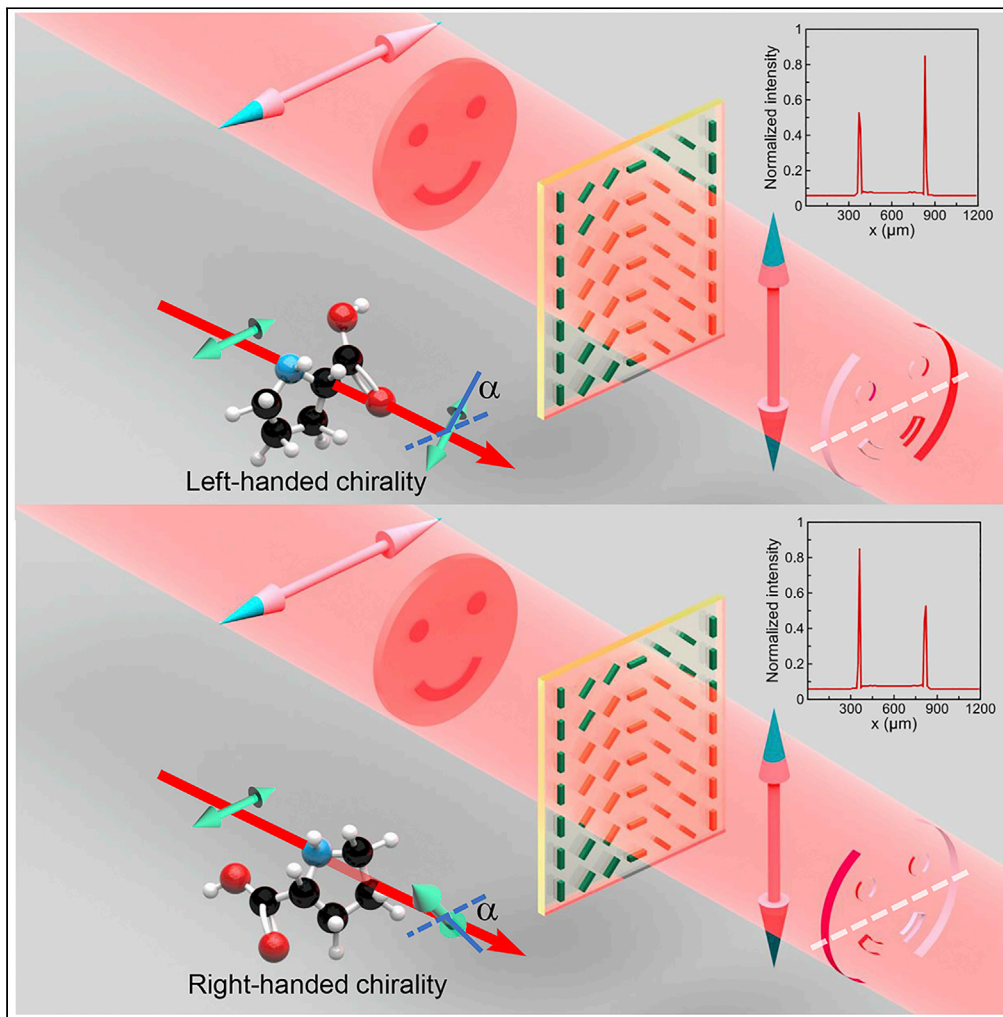**Article**

Computing metasurfaces enabled chiral edge image sensing

Ruisi Wang,
Shanshan He,
Shizhen Chen,
Weixing Shu,
Shuangchun Wen,
Hailu Luo

hailuluo@hnu.edu.cn

Highlights

Computing metasurfaces perform the spatial differentiation operations of phase object

Weak-value amplification technique has been proposed for the chiral sensing

The chiral edge image sensing has been demonstrated

Article

Computing metasurfaces enabled chiral edge image sensing

Ruisi Wang,[1] Shanshan He,[1] Shizhen Chen,[1] Weixing Shu,[1] Shuangchun Wen,[1] and Hailu Luo[1,2,*]

SUMMARY

Computing metasurfaces have shown the extraordinary ability to precisely perform optical analog operations to the input light wave, and therefore exhibit greater potentials toward sensing applications. Here, we propose a unique application of computing metasurface for chiral edge sensing by incorporating a weak-value amplification technique. The computing metasurface performs the spatial differentiation operations of phase objects and extracts the edge-enhanced images, because the phase gradient generally occurs at the edge. The chirality-induced polarization rotation acts as the preselection state and the spatial differentiation operations in the metasurface provide weak coupling. The amplified pointer shift related to the tiny polarization rotation will eventually lead to an asymmetric edge-enhanced image. Owing to the high sensitivity of the weak-value amplification, we experimentally demonstrate a high-contrast recognition of chirality by edge detection, which may have potential applications in real-time measurement and separation of chiral enantiomers.

INTRODUCTION

As one of the fundamental characteristics of biological molecules, chirality plays an essential role in living organisms (Sofikitis et al., 2014). There may be different physicochemical properties and functions between the two enantiomers (Lorenzo et al., 2000; Rhee et al., 2009; Cireasa et al., 2015). Owing to different physiological potencies and activities against living organisms, the recognition of enantiomers with opposite handedness is essential in food safety and drug synthesis (Hayat et al., 2015; Milner et al., 2019). Traditional approaches for enantiomer recognition of chirality molecules are polarimeters based on optical rotation but involving long tube and bulky devices. In addition, the polarimeters method only performs determination of optical rotation without intuitive observation of chiral objects. Therefore, fast recognition of chiral enantiomers and efficient image analysis of chiral objects such as chiral crystals still remain challenging.

Computing metasurfaces are two-dimensional artificial nanostructures capable of performing mathematical operations on the input electromagnetic field (Silva et al., 2014; Pors et al., 2015; Hwang and Davis, 2016; Zhu et al., 2017; Lee et al., 2017; Zangeneh-Nejad et al., 2020; Li et al., 2021; Jin et al., 2021; Yung et al., 2022; He et al., 2022; Fu et al., 2022). The spatial differentiation operations based on computing metasurfaces have been applied for all-optical image processing, especially for edge detection (Dong et al., 2018; Kwon et al., 2018; Zhou et al., 2019, 2020, 2021; Momeni et al., 2019; Huo et al., 2020; Liu et al., 2020; Wesemann et al., 2021; Solntsev et al., 2021; Yang et al., 2021). In recent years, because of the sensitivity to changes in physical parameters of the system, weak-value amplification techniques have been proposed for the chiral sensing (Rhee et al., 2013; Wang et al., 2020). The weak-value amplification technique is first introduced by Aharonov et al. (Aharonov et al., 1988; Dressel et al., 2014). There are three procedures generally involved: First, a measured system is prepared in the initial state $|\psi_i\rangle$. Then, the observable $\widehat{A}$ is very weakly coupled to the pointer state and produce an initial pointer shift Δx. Finally, the amplified pointer shift Δx_w is recorded when the system is postselected as a final state $|\psi_f\rangle$ (Jordan et al., 2014). The quantitative relationship between the amplified pointer shift and the initial shift is given by $\Delta x_w = A_w \Delta x$, and the weak value is obtained as

$$A_w = \frac{\langle \psi_f | \widehat{A} | \psi_i \rangle}{\langle \psi_f | \psi_i \rangle} \qquad \text{(Equation 1)}$$

If the preselection and postselection states are nearly orthogonal, $\langle \psi_f | \psi_i \rangle \rightarrow 0$, the final amplified pointer shift will be much greater than the initial pointer shift (Chen et al., 2015).

In this work, we propose computing metasurface for chiral edge image sensing by incorporating a weak-value amplification technique. By introducing this mechanism into chiral edge sensing, when there is a slight modification in the preselection state caused by optical rotation of chiral object, the initial shift will be significantly enhanced by the weak-value amplification, manifested as an asymmetric distribution of the output result, which makes weak-value amplification be a powerful tool for chiral edge image sensing. Chiral objects (L-proline and D-proline solution samples) with different concentrations are used to detect the feasibility and high contrast of the system. In our scheme, the preselection polarization state is modified by the optical rotation of the chiral object, but with the fixed postselection state. The Pancharatnam-Berry (PB) phase gradient introduced by the metasurface generates the spin-dependent shift. The amplified pointer shift related to the optical rotation angle exhibits a high sensitivity because of the weak-value amplification, which will eventually lead to an asymmetric edge-enhanced image. Combined with the advantages of computing metasurface and weak-value amplification techniques, our scheme enables fast identification of chiral objects, especially seeing the extraordinary edge images of chiral objects. Our scheme may provide potential applications in chemical and biological research, involving chirality recognition in a simpler, compact, high-sensitive way, and observation of the effects of chiral molecules solutions on cells or tissues via their edge-enhanced images.

RESULTS

The concept of optical differential operation

As shown in Figure 1, the light first propagates to the horizontal polarizer, then passes through the "smile" object and metasurface. After propagating to the analyzer, the left and right edges with asymmetric brightness are obtained. The chirality of the final edge is determined by the optical rotation of the chiral object. As an important characteristic of chiral molecules, optical rotation will result in a tiny rotation of the preselection state. Generally, the specific rotation used to identify the optical rotation ability of various chiral substances can be defined as follows: $[\alpha] = \frac{\alpha}{lc}$, where α is the optical rotation angle (in degrees), l and c are the thickness of the sample cell (in dm) and concentration of chiral solution (in g/mL), respectively (Wang et al., 2020). Here, the L-proline or D-proline solution filled in the "smile" shape is regarded as a chiral object. The bottom left corner insets in Figures 1A and 1B show optical rotation of left-handed substance and right-handed substance with the same value but the opposite direction, respectively.

With rotating the optical axis direction of GLP1 and QWP both along the x axis, we first consider the initial state after QWP in the spin basis without the chiral object

$$|\psi_i(x,y)\rangle = \frac{1-i}{2}[\psi_{in}(x,y)|+\rangle + \psi_{in}(x,y)|-\rangle] \qquad \text{(Equation 2)}$$

Here, $\psi_{in}(x,y)$ is the input wave function in position space and $|\pm\rangle$ are the spin basis. The optical axis direction in the metasurface is periodically varying in one dimension, e.g., $\varphi(x) = \Omega x$ where $\Omega = \pi/\Lambda$ is the spatial rotational rate of the optical axis, with Λ being the period (Ling et al., 2015). The theoretical far-field distribution of this metasurface is shown in Figure S1 (supplemental information). After passing through the metasurface, the left-handed and right-handed circularly polarized components will reverse its handedness and acquires an additional Pancharatnam-Berry phase $\Phi_{PB} = -2\sigma_{\pm}\varphi(x)$, with left-handed circularly polarized ($\sigma_+ = +1$) and right-handed circularly polarized ($\sigma_- = -1$) (see STAR Methods for the details of theoretical analysis). This space-variant Pancharatnam-Berry phase will lead to spin-dependent momentum shift in x direction, which could be given as

$$\Delta k_x = \sigma_{\pm}\frac{\partial \Phi_{PB}}{\partial x} = -2\sigma_{\pm}\frac{\pi}{\Lambda} \qquad \text{(Equation 3)}$$

The induced spatial shift in position space written as follows will increase linearly as propagation distance z increased

$$\Delta x = \frac{\Delta k_x z}{k_0} = -\sigma_{\pm}\frac{\lambda z}{\Lambda} \qquad \text{(Equation 4)}$$

where $k_0 = \frac{2\pi}{\lambda}$ is the vacuum wave vector. Therefore, the output field after metasurface can be given as

$$|\psi_m(x,y) = \frac{1-i}{2}[\psi_{in}(x+\Delta x,y)|+\rangle + \psi_{in}(x-\Delta x,y)]|-\rangle, \qquad \text{(Equation 5)}$$

which means that the left-handed and right-handed circularly polarized components will ultimately experience Δx shift in opposite directions. By setting optical axis direction of GLP2 along y direction, the linear
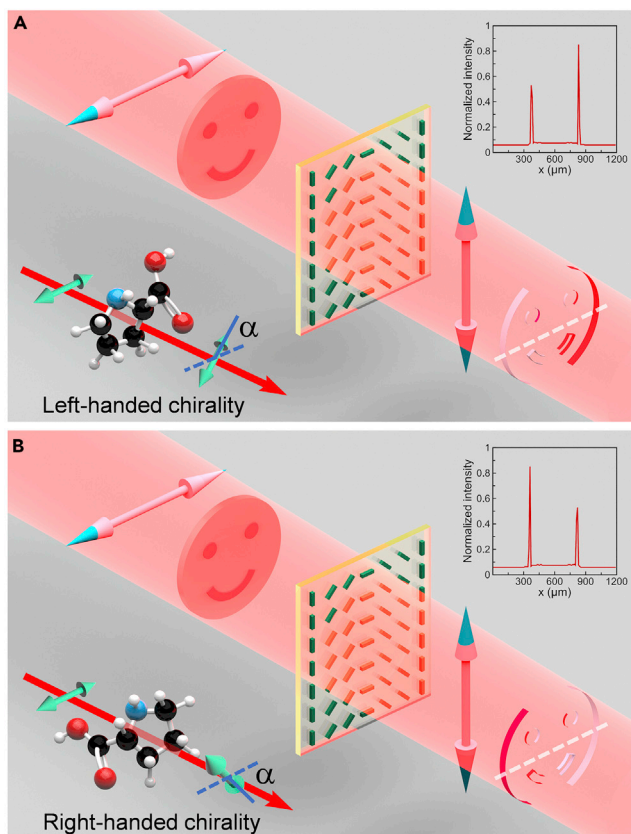
Figure 1. Schematic illustration of the chiral edge sensing

(A) The polarized incident light passes through the object with left-handed chirality, then the beam spin-dependent splitting occurs because of the phase gradient of the metasurface. Finally, the edge image with right-part brighter than the left-part is obtained after an analyzer orthogonal to the first polarizer. The inset in bottom left corner shows that polarization plane of light will rotate when a linearly polarized light passes through left-handed substance. The inset in upper right corner shows theoretical intensity curve corresponding to the white dashed line in the final image for the positive optical rotation angle.

(B) Schematic figure of the edge imaging for the object with right-handed chirality. Here, the edge image with left-part brighter than the right-part is obtained. The inset in bottom left corner shows that polarization plane of light will rotate when a linearly polarized light passes through right-handed substance. The inset in upper right corner shows theoretical intensity curve corresponding to the white dashed line in the final image for the negative optical rotation angle.

polarization caused by the overlapped two orthogonal circular polarizations will be eliminated, but still preserving edge information. The final output field can be written as

$$|\psi_f(x,y)\rangle = \frac{1+i}{2}[\psi_{in}(x+\Delta x, y) - \psi_{in}(x-\Delta x, y)]\mathbf{e_y} \qquad \text{(Equation 6)}$$

Then Equation (6) can be further simplified to the following form due to Δx is extremely small compared with the field distribution.

$$\psi_f(x,y) \simeq 2\Delta x \frac{\partial \psi_{in}(x,y)}{\partial x}\mathbf{e_y} \qquad \text{(Equation 7)}$$

It is shown that our proposed mechanism can achieve the spatial differentiation of the input field, which enables one-dimensional edge detection for objects.

Weak-value amplification in chiral edge detection

In order to achieve chiral edge detection, the weak-value amplification technique with high precision is applied, generally involving three steps: preselection, weak interaction, and postselection on a final quantum state. In our scheme, the preselected polarization state is modified by optical rotation of the chiral

object, and the metasurface provides the weak interaction. First, the initial state can be written as (Chen et al., 2015)

$$|\Phi_i\rangle \;=\; \int dx\varphi(x)|x\rangle|\psi_i\rangle \;=\; \int dk_x\psi(k_x)|k_x\rangle|\psi_i\rangle \qquad \text{(Equation 8)}$$

where $|\psi_i\rangle$ is the preselection state and $\psi(k_x)$ is the Fourier transform of the incident Gaussian light $\varphi(x)$ which can be specified by

$$\varphi(x) \;=\; \left(\frac{2}{w^2\pi}\right)^{\frac{1}{4}} e^{-\frac{x^2}{w^2}} \qquad \text{(Equation 9)}$$

where w is the width of the wave function. In this work, we assume that the incident beam propagates along the z axis, and the metasurface is parallel to the xy plane. For simplicity, the x-distribution of the incident light is considered to be a Gaussian distribution. In our weak measurements scheme, the metasurface provides the weak coupling. The enhancement effect is achieved by preselecting and postselecting the polarization states of the incoming photons in states $|\psi_i\rangle$ and $|\psi_f\rangle$. For generating the spin-dependent splitting with different k vectors, the observable of the system is weakly coupled with the meter via the interaction Hamiltonian given by $\widehat{H} \;=\; \Delta k_x \widehat{A} x$. The observable $\widehat{A}$ is the Pauli operator. Therefore, the initial state develops as

$$|\Psi\rangle \;=\; e^{-i\int \widehat{H}dt} \int dx\varphi(x)|x\rangle|\psi_i\rangle \qquad \text{(Equation 10)}$$

Here, the transverse spatial distribution in state $|x\rangle$ is regarded as the meter. Then the preselected state $|\psi_i\rangle$ and the postselected state $|\psi_f\rangle$ are written as

$$|\psi_i\rangle \;=\; \frac{1-i}{\sqrt{2}}\left[\cos\left(\alpha - \frac{\pi}{4}\right)|+\rangle + \cos\left(\alpha + \frac{\pi}{4}\right)|-\rangle\right] \qquad \text{(Equation 11)}$$

$$|\psi_f\rangle \;=\; \frac{i}{\sqrt{2}}(|-\rangle - |+\rangle) \qquad \text{(Equation 12)}$$

In our scheme, the preselection is realized by the combination of GLP1, optical rotation angle α from the chiral object, and QWP. For different chiral objects, the preselection could be modified by the variability of the optical rotation angle. The process of introducing preselection and postselection actually establishes a quantitative relationship between the amplified output result and the initial small signal, which is named weak value of the measured observable (see STAR Methods for the details of theoretical analysis)

$$A_w \;=\; \frac{\langle\psi_f|\widehat{A}|\psi_i\rangle}{\langle\psi_f|\psi_i\rangle} = \cot\alpha \qquad \text{(Equation 13)}$$

Therefore, after the interaction Hamiltonian, the initial state becomes

$$|\Psi\rangle \;=\; \frac{1-i}{\sqrt{2}}\int dx\varphi(x)|x\rangle e^{i\Delta k_x x}\cos\left(\alpha - \frac{\pi}{4}\right)|+\rangle + dx\varphi(x)|x\rangle e^{-i\Delta k_x x}\cos\left(\alpha + \frac{\pi}{4}\right)|-\rangle \qquad \text{(Equation 14)}$$

After the postselection of state, the wave function evolves to the final state

$$\langle\psi_f|\Psi\rangle \;=\; \frac{1+i}{2}\int - dx\varphi(x)|x\rangle e^{i\Delta k_x x}\cos\left(\alpha - \frac{\pi}{4}\right) + dx\varphi(x)|x\rangle e^{-i\Delta k_x x}\cos\left(\alpha + \frac{\pi}{4}\right) \qquad \text{(Equation 15)}$$

Finally, the weak-value amplified pointer shift can be obtained as (Chen et al., 2015)

$$\Delta x_w \;=\; A_w^{mod}\Delta x, \qquad \text{(Equation 16)}$$

where A_w^{mod} is the modified weak value

$$A_w^{mod} \;=\; \frac{e^{2(w\pi/\Lambda)^2}\sin 2\alpha}{\cos 2\alpha - e^{2(w\pi/\Lambda)^2}}. \qquad \text{(Equation 17)}$$

Here, α is the optical rotation angle attributed to the chiral objects and the concentration of the solution. In Figure 2A, the modified weak values for three different computing metasurfaces with periods $\Lambda = 4$ mm, $\Lambda = 8$ mm, $\Lambda = 16$ mm are shown. The modified weak values as functions of metasurface periods with three preselected angles are obtained in Figure 2B. According to Equation (16), there is a quantitative relationship between amplified pointer shifts and the preselection polarization state shown in Figure 2C ($\Lambda = 8$ mm). The asymmetric splitting beam distribution caused by slight changes in the preselected states will lead to
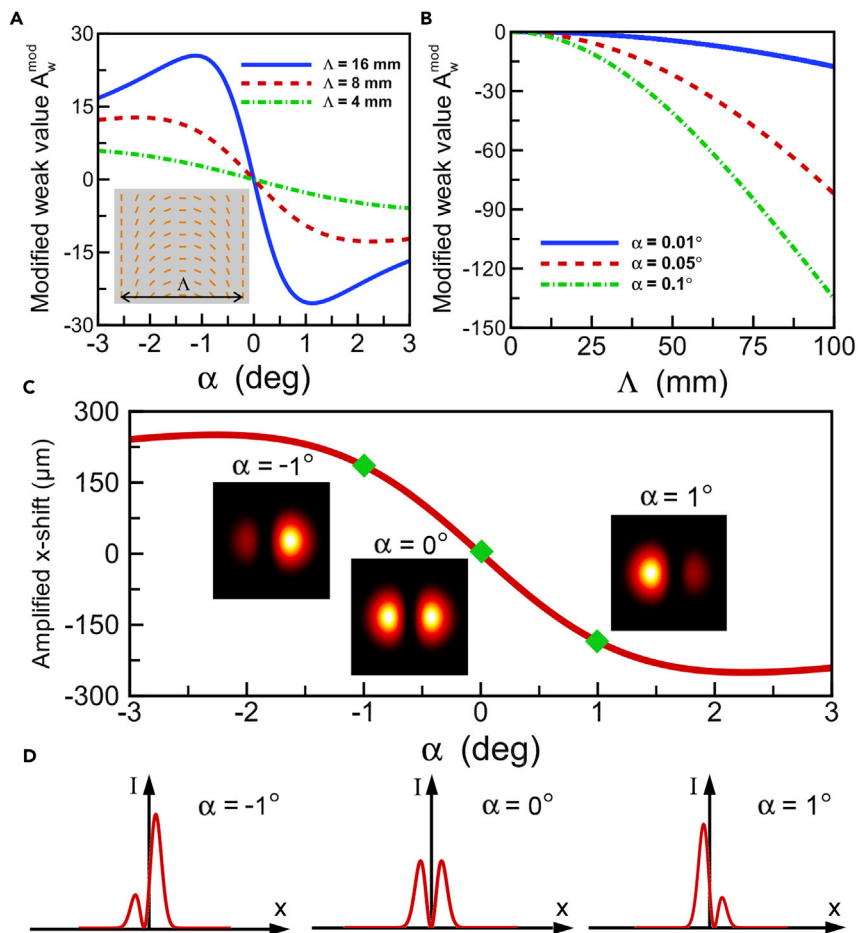
Figure 2. Weak-value amplification

(A) Modified weak values as functions of preselected angles when the metasurface periods $\varLambda$ are taken as 4mm, 8mm, 16mm, respectively. The inset is theoretical distribution of local optical slow-axis orientation of the metasurface.

(B) Modified weak values as functions of metasurface periods when the preselected angles α are taken as 0.01°, 0.05°, 0.1°, respectively.

(C) The relationship between amplified beam shifts and preselected angles in the case of z = 250 mm. The three special points indicate the theoretical output intensity of the light corresponding to $\alpha = -1°$, $\alpha = 0°$, $\alpha = 1°$, respectively.

(D) The intensity curves along the central axis x direction in three insets of (C), respectively.

brightness differences for edge detection of chiral objects. Figure 2D is the intensity curves along the central axis x direction corresponding to the three insets shown from left to right in Figure 2C, respectively.

Spatial spectral transfer function

To illustrate the optical differentiation effect, we experimentally measured the transfer function of the metasurface. As shown in Figure 3A, the horizontal direction linearly polarized beam produced by GLP1 passes through QWP with the same optical axis as GLP1. Then the beam will be focused on the metasurface by L1. GLP2 is used to analyze the splitting beam spot. The distance between L1 and L2 is the sum of their focal lengths and the CCD is placed at the real focal plane of L2 to collect the output beam. The metasurface is fabricated by the femtosecond laser writing of self-assembled nanogratings inside a fused silica glass (Beresna et al., 2011). A periodic pattern with space-variant optical axis direction is formed inside the nanostructures under strong laser irradiation (see STAR Methods for the details of sample fabrication). For this metasurface sample, the optical transmission efficiency of 93.2% and conversion efficiency of 95.7% are measured at the wavelength of 632.8 nm. The left inset in Figure 3A shows the local optical slow-axis orientation of this metasurface ($\varLambda$ =8 mm) measured by polariscefopic analysis. The right inset in Figure 3A
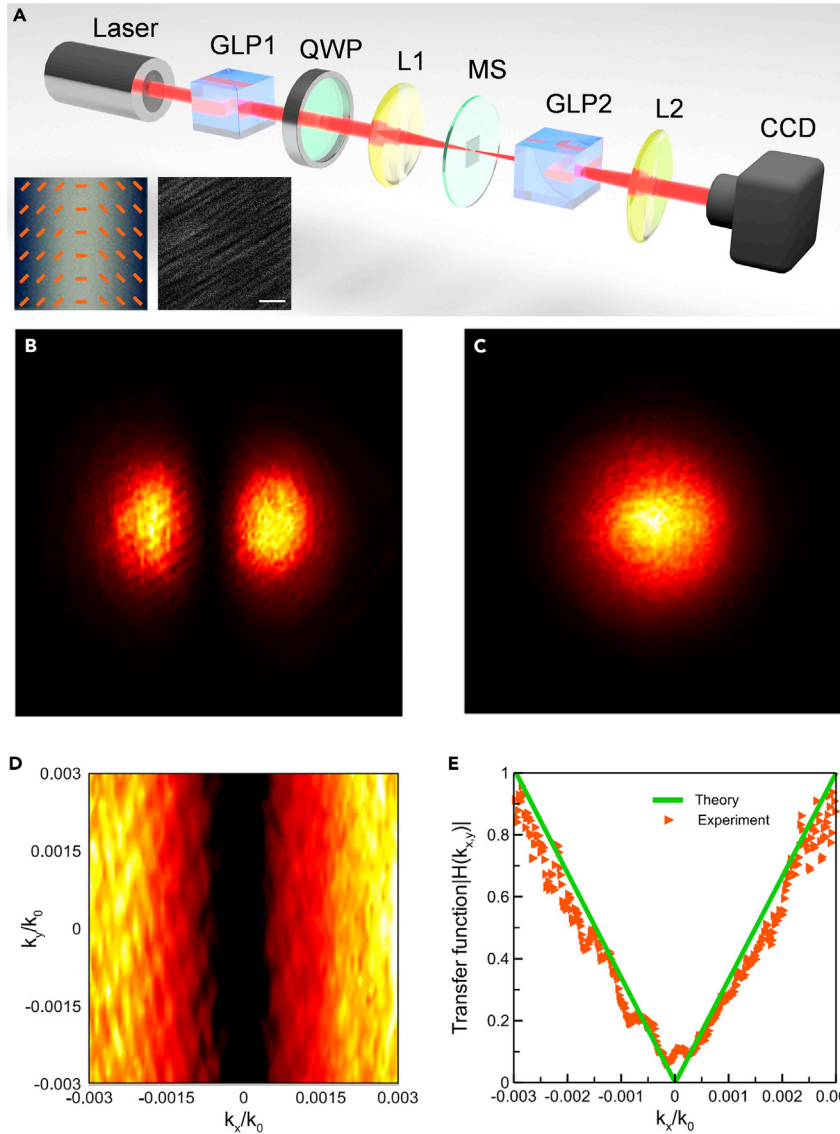
Figure 3. Measurement of the spatial transfer function of the mentioned spatial differentiator

(A) Experiment setup: Laser (He-Ne laser, 632.8 nm wavelength); L1 and L2, lens with focal length 175mm and 250mm, respectively; GLP1 and GLP2, a pair of crossed Glan laser polarizers; QWP, quarter-wave plate; Metasurface, period 8 mm; CCD, charge-coupled device. The left inset shows the characterization of the metasurface utilized by crossed linear polarizers. The orange bars indicate local optical slow-axis orientation of the metasurface. The right inset is the scanning electron microscope image of the metasurface sample (Scale bar, 100 nm).

(B and C) The experimental intensity distribution with and without the spatial differentiator, respectively.

(D) The measured results of spatial spectral transfer function.

(E) The theory and experiment results of the transfer function for $k_y = 0$.

presents a scanning electron microscope (SEM) image of the metasurface sample. To measure the transfer function $H(k_x, k_y)$, we first record the intensity distribution $I_{out}(x, y)$ after the 4f system (Figure 3B) and calculate the electrical field distribution based on $E_{out}(x, y) = \sqrt{I_{out}(x, y)}$. Then we measure the intensity distribution $I_{in}(x, y)$ before L1, as shown in Figure 3C. The electrical field distribution $E_{in}(x, y)$ is also obtained. The final transfer function can be described by

$$H(k_x, k_y) = \frac{\tilde{E}_{out}(k_x, k_y)}{\tilde{E}_{in}(k_x, k_y)}$$
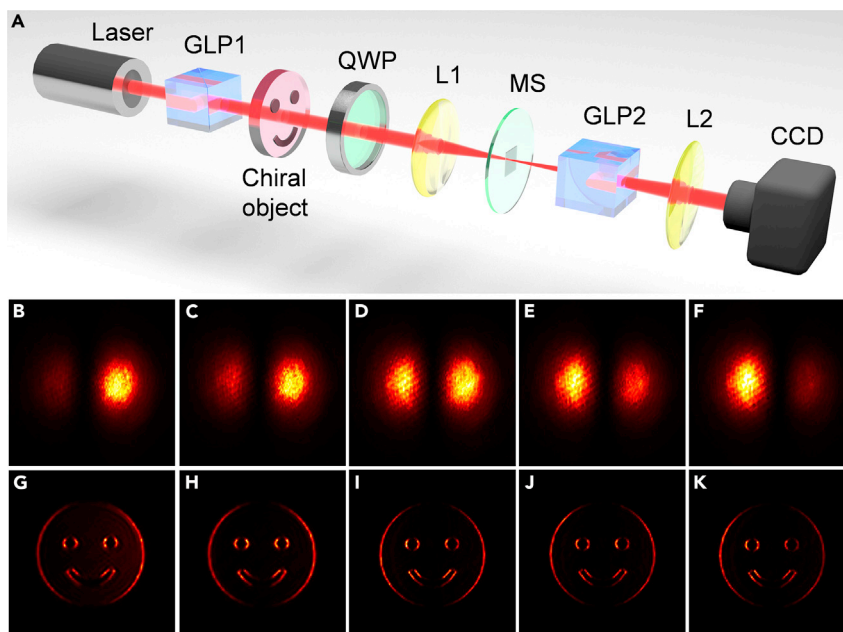
(Equation 18)

Figure 4. Experimental demonstration of chiral edge image sensing

(A) Schematic of the experimental setup for chiral edge detection.

(B and C) The output intensity of the light in the case of using a quartz cuvette loaded with L-proline solution. Here, the concentration for (B) and (C) are 0.1 g/mL, 0.05 g/mL.

(D) The output intensity of the light without the proline solution.

(E and F) The output intensity of the light in the case of using a quartz cuvette loaded with D-proline solution. Here, the concentration for (E) and (F) are 0.05 g/mL, 0.1 g/mL.

(G–K) The measured images in the case of using chiral "smile" object loaded with proline solution at the same concentration corresponding to the first row.

where $\tilde{E}(k_x, k_y)$ is the Fourier transform of $E(x, y)$. The phase distribution for the spatial spectral transfer function is depicted in Figure S3 (supplemental information). After processing data extracted from Figures 3B and 3C, the measured transfer function is demonstrated as shown in Figure 3D. To clearly evaluate the detailed features, we plot the experimental transfer function when $k_y/k_0 = 0$ (Figure 3E), which shows linear correlation of k_x and illustrates that the spatial differentiation along x direction can be well proved.

Detection of the object chirality

Then we employ the mentioned weak measurements technique and the metasurface sample to realize the chirality recognition. The experimental setup is schematically shown in Figure 4A, where the light comes from a He-Ne laser, and then the horizontal linear polarized beam obtained by GLP1 passes through the chiral object loaded with a certain concentration of proline solution. The optical activity of the chiral solution makes the polarization plane rotate a small angle, which can be regarded as the preselection state in combination with GLP1 and QWP. Here, L1 and L2 construct the 4f imaging system. After impinging onto the metasurface, the splitting LCP and RCP components pass the analyzer (GLP2) and finally the edge image will be recorded by the CCD. The analyzer GLP2 builds a postselection state $|V\rangle$.

Now we demonstrate the superiority of our scheme in chiral edge image sensing. For chiral solutions with different concentrations, the corresponding optical rotation angles will lead to different preselection states, which will eventually result in beam asymmetry after passing through the whole system. To clearly illustrate the effect of chiral solutions with different concentrations on output beam, we first place a 3 cm thickness quartz cuvette with L-proline solution (Figures 4B and 4C) and D-proline solution (Figures 4E and 4F) at the front focal length of L1 and the beam intensities are recorded on CCD (see STAR Methods for the details of sample preparation and experimental measurements). As the concentration increases, we find that the symmetric double-peak distribution gradually changes to asymmetric distribution with the
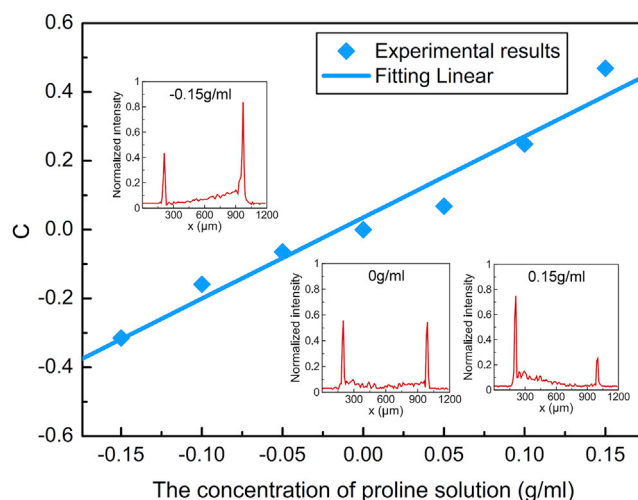
Figure 5. The relationship between the peak-contrast-ratio pointer and the concentration of proline solution
The negative concentration represents L-proline solution, while the positive concentration represents D-proline solution.
The three insets from left to right show intensity curves corresponding to the horizontal central axis across the edge
images, which are measured at 0.15 g/mL L-proline solution, without proline solution, and 0.15 g/mL D-proline solution.,
respectively.

asymmetry degree getting stronger. Then we replace the quartz cuvette with a chiral "smile" object (3 cm
thickness) loaded with the same increasing concentrations of L-proline solution and D-proline solution, cor-
responding to Figures 4G–4K, respectively. The highest resolution of the detected edge is around 6 μm in
Figure 4K. We note that for left-handed objects, the edge of the right side is brighter than the left side. As
the solution concentration increases, the contrast of left-side and right-side edges gets obvious gradually.
Similarly, for right-handed objects, the opposite phenomenon is observed, where the brightness of the left-
side edge is stronger than the right side.

For an intuitive comparison, we extract the light intensity of each pixel on the horizontal central axis across
the edge images and the two maximum points are obtained. The peak-contrast-ratio pointer can be
defined by

$$C = \frac{I_L - I_R}{I_L + I_R} \qquad \text{(Equation 19)}$$

Here, I_L is the light intensity of the left maximum point and I_R is the light intensity of the right maximum
point. After calculating the peak-contrast-ratio pointer of the L-proline and D-proline solution both at
the concentration of 0.05 g/mL, 0.1 g/mL, and 0.15 g/mL, respectively, the relationship between the
peak-contrast-ratio pointer and the concentration of proline solution can be obtained in Figure 5.

We measured the corresponding amplified shifts $\varDelta x_w$ are 153.8 μm, 231.3 μm, 250.2 μm. According to
Equation (16), we finally obtained the modified weak value A_w are 7.78, 11.70, 12.65 for the L-proline solu-
tion at concentration of 0.05 g/mL, 0.1 g/mL, 0.15 g/mL respectively. The corresponding optical rotation
angles for these three concentrations are 0.776°, 1.509°, 2.138°, respectively. Under direct detection of
the polarization rotation, we also obtain polarization rotation angles for 0.05 g/mL, 0.1 g/mL, and 0.15
g/mL are 0.76°, 1.52°, 2.12°. Here, the high measurement resolution with 10^{-3} degree is achieved in the
proposed approach in this paper, which outperforms the traditional polarimeter 10^{-2} degree. For the
D-proline solution at concentration of 0.05 g/mL, 0.1 g/mL, 0.15 g/mL, the measured amplified shifts are
-157.7 μm, -235.1 μm, and -250.1 μm, respectively. Then we obtain the corresponding optical rotation
angles are 0.802°, 1.577°, and 2.124°. Optical rotation will cause the change of preselection state, which
determines the weak-value amplification. This will result in a significant shift of the beam center of gravity.
Ultimately, the edge imaging of the chiral object shows an asymmetry because of the asymmetric beam
distribution. Weak measurement techniques have had great applications in biosensing in recent years,
especially for high-precision detection. By combining weak measurements with the imaging system, our

proposed scheme not only can be used to identify molecular chirality, but also perform edge imaging with left and right brightness discrimination for chiral objects with different optical rotations.

DISCUSSION

In conclusion, we have demonstrated enantiomers recognition and optical edge detection of chiral objects based on weak measurement schemes. In our scheme, the preselected polarization state is modified by optical rotation of the chiral object and the optical edge detection is achieved by the metasurface. Based on the interaction between spin-orbit coupling mechanism, the metasurface can manipulate the input field for phase and polarization distribution and thereby shows great application advantages in high-contrast edge imaging. The optical activity of the chirality sample can be detected by the final edge image and the edge contrast varies with the concentration of the chiral solution. Due to high sensitivity to small changes of the system, weak measurements can serve as a powerful tool for detecting small beam deflection caused by the optical rotation of a chiral object on the condition that the spatial beam separation magnitude is much smaller than the beam diameter itself.

By incorporating the superiority of metasurface and weak measurements technique, there are two appealing features for the mentioned scheme: it does not involve any complex and bulky devices compared to traditional polarimeter methods, and the edge image will be more intuitive by filtering out unnecessary information while maintaining significant geometric elements. The proposed scheme exhibits the advantages of high efficiency, compact type, and high resolution. It is believed that our results may provide a simple and accurate method for identification and analysis of chiral objects, which may have potential applications in real-time chemical and biological reaction.

Limitations of the study

The inaccuracy of femtosecond laser writing technology may cause the minor error of metasurface optical axis distribution, which will lead to slight deformation between the theoretical and experimental spatial transfer functions. In our experiment, the weak-value amplification is not large enough due to the small period of the metasurface sample, but large weak values can be obtained in principle as the designed period increases (see Figure S2 in supplemental information). In addition, the chiral image sensing is limited to one dimension. It would be able to be extended to two dimensions with high-order differentiation (Liu et al., 2022), by designing the computing metasurface.

STAR★METHODS

Detailed methods are provided in the online version of this paper and include the following:

- KEY RESOURCES TABLE
- RESOURCE AVAILABILITY
  - Lead contact
  - Materials availability
  - Data and code availability
- METHOD DETAILS
  - Theoretical analysis
  - Sample fabrication
  - Sample preparation
  - Experimental measurements

SUPPLEMENTAL INFORMATION

Supplemental information can be found online at https://doi.org/10.1016/j.isci.2022.104532.

REFERENCES

Aharonov, Y., Albert, D.Z., and Vaidman, L. (1988). How the result of a measurement of a component of the spin of a spin-1/2 particle can turn out to be 100. Phys. Rev. Lett. *60*, 1351–1354. https://doi.org/10.1103/physrevlett.60.1351.

Beresna, M., Gecevičius, M., Kazansky, P.G., and Gertus, T. (2011). Radially polarized optical vortex converter created by femtosecond laser nanostructuring of glass. Appl. Phys. Lett. *98*, 201101. https://doi.org/10.1063/1.3590716.

Chen, S., Zhou, X., Mi, C., Luo, H., and Wen, S. (2015). Modified weak measurements for the detection of the photonic spin Hall effect. Phys. Rev. *91*, 062105. https://doi.org/10.1103/physreva.91.062105.

Cireasa, R., Boguslavskiy, A.E., Pons, B., Wong, M.C.H., Descamps, D., Petit, S., Ruf, H., Thiré, N., Ferré, A., Suarez, J., et al. (2015). Probing molecular chirality on a sub-femtosecond timescale. Nat. Phys. *11*, 654–658. https://doi.org/10.1038/nphys3369.

Dong, Z., Si, J., Yu, X., and Deng, X. (2018). Optical spatial differentiator based on subwavelength high-contrast gratings. Appl. Phys. Lett. *112*, 181102. https://doi.org/10.1063/1.5026309.

Dressel, J., Malik, M., Miatto, F.M., Jordan, A.N., and Boyd, R.W. (2014). Colloquium: understanding quantum weak values: basics and applications. Rev. Mod. Phys. *86*, 307–316. https://doi.org/10.1103/revmodphys.86.307.

Fu, W., Zhao, D., Li, Z., Liu, S., Tian, C., and Huang, K. (2022). Ultracompact meta-imagers for arbitrary all-optical convolution. Light Sci. Appl. *11*, 62. https://doi.org/10.1038/s41377-022-00752-5.

Hayat, A., Mueller, J.P.B., and Capasso, F. (2015). Lateral chirality-sorting optical forces. Proc. Natl. Acad. Sci. U S A. *112*, 13190–13194. https://doi.org/10.1073/pnas.1516704112.

He, S., Wang, R., and Luo, H. (2022). Computing metasurfaces for all-optical image processing: a brief review. Nanophotonics *11*, 1083–1108. https://doi.org/10.1515/nanoph-2021-0823.

Huo, P., Zhang, C., Zhu, W., Liu, M., Zhang, S., Zhang, S., Chen, L., Lezec, H.J., Agrawal, A., Lu, Y., and Xu, T. (2020). Photonic spin-multiplexing metasurface for switchable spiral phase contrast imaging. Nano Lett. *20*, 2791–2798. https://doi.org/10.1021/acs.nanolett.0c00471.

Hwang, Y., and Davis, T.J. (2016). Optical metasurfaces for subwavelength difference operations. Appl. Phys. Lett. *109*, 181101. https://doi.org/10.1063/1.4966666.

Jin, J., Li, X., Pu, M., Guo, Y., Gao, P., Xu, M., Zhang, Z., and Luo, X. (2021). Angular-multiplexed multichannel optical vortex arrays generators based on geometric metasurface. iScience *24*, 102107. https://doi.org/10.1016/j.isci.2021.102107.

Jordan, A.N., Martínez-Rincón, J., and Howell, J.C. (2014). Technical advantages for weak-value amplification: when less is more. Phys. Rev. X *4*, 011031. https://doi.org/10.1103/physrevx.4.011031.

Kwon, H., Sounas, D., Cordaro, A., Polman, A., and Alù, A. (2018). Nonlocal metasurfaces for optical signal processing. Phys. Rev. Lett. *121*, 173004. https://doi.org/10.1103/physrevlett.121.173004.

Lee, Y., Kim, S.J., Park, H., and Lee, B. (2017). Metamaterials and metasurfaces for sensor applications. Sensors *17*, 1726. https://doi.org/10.3390/s17081726.

Li, Z., Deng, L., Deng, J., He, Z., Tao, J., Zheng, G., and Yu, S. (2021). Metasurface-enabled three-in-one nanoprints by multifunctional manipulations of light. iScience *24*, 103510. https://doi.org/10.1016/j.isci.2021.103510.

Ling, X., Zhou, X., Yi, X., Shu, W., Liu, Y., Chen, S., Luo, H., Wen, S., and Fan, D. (2015). Giant photonic spin Hall effect in momentum space in a structured metamaterial with spatially varying birefringence. Light Sci. Appl. *4*, e290. https://doi.org/10.1038/lsa.2015.63.

Liu, J., Yang, Q., Chen, S., Xiao, Z., Wen, S., and Luo, H. (2022). Intrinsic optical spatial differentiation enabled quantum dark-field microscopy. Phys. Rev. Lett. *128*, 193601. https://doi.org/10.1103/physrevlett.128.193601.

Liu, W., Li, Z., Cheng, H., and Chen, S. (2020). Dielectric resonance-based optical metasurfaces: from fundamentals to applications. iScience *23*, 101868. https://doi.org/10.1016/j.isci.2020.101868.

Lorenzo, M.O., Baddeley, C.J., Muryn, C., and Raval, R. (2000). Extended surface chirality from supramolecular assemblies of adsorbed chiral molecules. Nature *404*, 376–379. https://doi.org/10.1038/35006031.

Milner, A.A., Fordyce, J.A.M., MacPhail-Bartley, I., Wasserman, W., Milner, V., Tutunnikov, I., and Averbukh, I.S. (2019). Controlled enantioselective orientation of chiral molecules with an optical centrifuge. Phys. Rev. Lett. *122*, 223201. https://doi.org/10.1103/physrevlett.122.223201.

Momeni, A., Rajabalipanah, H., Abdolali, A., and Achouri, K. (2019). Generalized optical signal processing based on multioperator metasurfaces synthesized by susceptibility tensors. Phys. Rev. Appl. *11*, 064042. https://doi.org/10.1103/physrevapplied.11.064042.

Pors, A., Nielsen, M.G., and Bozhevolnyi, S.I. (2015). Analog computing using reflective plasmonic metasurfaces. Nano Lett. *15*, 791–797. https://doi.org/10.1021/nl5047297.

Rhee, H., Choi, J.S., Starling, D.J., Howell, J.C., and Cho, M. (2013). Amplifications in chiroptical spectroscopy, optical enantioselectivity, and weak value measurement. Chem. Sci. *4*, 4107. https://doi.org/10.1039/c3sc51255j.

Rhee, H., June, Y.G., Lee, J.S., Lee, K.K., Ha, J.H., Kim, Z.H., Jeon, S.J., and Cho, M. (2009). Femtosecond characterization of vibrational optical activity of chiral molecules. Nature *458*, 310–313. https://doi.org/10.1038/nature07846.

Silva, A., Monticone, F., Castaldi, G., Galdi, V., Alù, A., and Engheta, N. (2014). Performing mathematical operations with metamaterials. Science *343*, 160–163. https://doi.org/10.1126/science.1242818.

Sofikitis, D., Bougas, L., Katsoprinakis, G.E., Spiliotis, A.K., Loppinet, B., and Rakitzis, T.P. (2014). Evanescent-wave and ambient chiral sensing by signal-reversing cavity ringdown polarimetry. Nature *514*, 76–79. https://doi.org/10.1038/nature13680.

Solntsev, A.S., Agarwal, G.S., and Kivshar, Y.S. (2021). Metasurfaces for quantum photonics. Nat. Photonics *15*, 327–336. https://doi.org/10.1038/s41566-021-00793-z.

Wang, R., Zhou, J., Zeng, K., Chen, S., Ling, X., Shu, W., Luo, H., and Wen, S. (2020). Ultrasensitive and real-time detection of chemical reaction rate based on the photonic spin Hall effect. APL Photonics 5, 016105. https://doi.org/10.1063/1.5131183.

Wesemann, L., Davis, T.J., and Roberts, A. (2021). Meta-optical and thin film devices for all-optical

information processing. Appl. Phys. Rev. *8*, 031309. https://doi.org/10.1063/5.0048758.

Yang, H., Xie, Z., He, H., Zhang, Q., Li, J., Zhang, Y., and Yuan, X. (2021). Switchable imaging between edge-enhanced and bright-field based on a phase-change metasurface. Opt. Lett. *46*, 3741. https://doi.org/10.1364/ol.428870.

Yung, T.K., Xi, J., Liang, H., Lau, K.M., Wong, W.C., Tanuwijaya, R.S., Zhong, F., Liu, H., Tam, W.Y., and Li, J. (2022). Polarization coincidence images from metasurfaces with HOM-type interference. iScience *25*, 104155. https://doi.org/10.1016/j.isci.2022.104155.

Zangeneh-Nejad, F., Sounas, D.L., Alù, A., and Fleury, R. (2020). Analogue computing with metamaterials. Nat. Rev. Mater. *6*, 207–225. https://doi.org/10.1038/s41578-020-00243-2.

Zhou, J., Qian, H., Chen, C.F., Zhao, J., Li, G., Wu, Q., Luo, H., Wen, S., and Liu, Z. (2019). Optical edge detection based on high-efficiency dielectric metasurface. Proc. Natl. Acad. Sci. U S A. *116*, 11137–11140. https://doi.org/10.1073/pnas.1820636116.

Zhou, J., Qian, H., Zhao, J., Tang, M., Wu, Q., Lei, M., Luo, H., Wen, S., Chen, S., and Liu, Z.

(2021). Two-dimensional optical spatial differentiation and high-contrast imaging. Natl. Sci. Rev. *8*, nwaa176. https://doi.org/10.1093/nsr/nwaa176.

Zhou, Y., Zheng, H., Kravchenko, I.I., and Valentine, J. (2020). Flat optics for image differentiation. Nat. Photonics *14*, 316–323. https://doi.org/10.1038/s41566-020-0591-3.

Zhu, T., Zhou, Y., Lou, Y., Ye, H., Qiu, M., Ruan, Z., and Fan, S. (2017). Plasmonic computing of spatial differentiation. Nat. Commun. *8*, 15391. https://doi.org/10.1038/ncomms15391.

STAR★METHODS

KEY RESOURCES TABLE

REAGENT or RESOURCE	SOURCE	IDENTIFIER
Other		
He-Ne Laser	Thorlabs company	HNL210LB
CCD	Thorlabs company	CS165CU

RESOURCE AVAILABILITY

Lead contact
Any further information and requests for resources and materials should be directed to and will be fulfilled by the lead contact, Prof. Hailu Luo (hailuluo@hnu.edu.cn).

Materials availability
This study did not generate new unique reagents.

Data and code availability
- Data reported in this paper will be shared by the lead contact upon request.
- This paper does not report original code.
- Any additional information required to reanalyze the data reported in this paper is available from the lead contact upon request.

METHOD DETAILS

Theoretical analysis
1. The principle of metasurface

The designed metasurface with the phase retardation π has a periodically varying optical axis along the x direction, which makes the phase gradient also vary along the x axis. By employing Jones matrix, it is convenient to describe the metasurface:

$$T = \begin{bmatrix} \cos 2\varphi & \sin 2\varphi \\ \sin 2\varphi & -\cos 2\varphi \end{bmatrix} \tag{Equation 20}$$

Here, $\varphi(x) = \frac{\pi x}{\Lambda}$ is local optical axis direction. When the left-handed circularly polarized light $|L\rangle$ or the right-handed circularly polarized light $|R\rangle$ is vertically impinges onto the metasurface, the output state can be expressed as

$$|E_{out}\rangle = T(x,y)|L\rangle = \exp(i2\varphi)|R\rangle \tag{Equation 21}$$
$$|E_{out}\rangle = T(x,y)|R\rangle = \exp(-i2\varphi)|L\rangle \tag{Equation 22}$$

The above two equations reveal that the metasurface with the phase retardation π can invert the handedness of the incident photon and introduce an additional space-variant phase, which is called PB phase (Pancharatnam-Berry phase).

2. Calculation of weak value

We assume the preselection state of the measuring system is $|\psi_i\rangle$, which is realized by the combination of a Glan laser polarizer (GLP1), optical rotation angle α from the chiral object, and a quarter wave plate (QWP). As we know, for an arbitrary phase retarder, it is convenient to employ the Jones matrix to describe the light propagation property when passing through it:

$$V(\varphi) = R(-\varphi)W_0 R(\varphi) \tag{Equation 23}$$

$R(\varphi) = \begin{bmatrix} \cos\varphi & \sin\varphi \\ -\sin\varphi & \cos\varphi \end{bmatrix}$ is the coordinate-dependent matrix, $W_0 = \begin{bmatrix} \exp(-i\Gamma/2) & 0 \\ 0 & \exp(i\Gamma/2) \end{bmatrix}$ is the Jones matrix of a uniaxial crystal. We consider the orientation of the quarter-wave plate is $\varphi = 0$, with its fast-axis parallel to the GLP1. Here, for QWP, $\Gamma = \frac{\pi}{2}$. Then Jones matrix could be written as:

$$V_{QWP} = \begin{bmatrix} \dfrac{1-i}{\sqrt{2}} & 0 \\ 0 & \dfrac{1+i}{\sqrt{2}} \end{bmatrix} \tag{Equation 24}$$

The preselection state could be given by:

$$\psi_i = V_{QWP}E_{input} = \begin{bmatrix} \dfrac{1-i}{\sqrt{2}} & 0 \\ 0 & \dfrac{1+i}{\sqrt{2}} \end{bmatrix}\begin{bmatrix} \cos\alpha \\ \sin\alpha \end{bmatrix} = \begin{bmatrix} \dfrac{(1-i)\cos\alpha}{\sqrt{2}} \\ \dfrac{(1+i)\sin\alpha}{\sqrt{2}} \end{bmatrix} \tag{Equation 25}$$

Here, $\begin{bmatrix} \cos\alpha \\ \sin\alpha \end{bmatrix}$ represents the field after the GLP1 and chiral object, which is α linear polarization with x axis. In the spin basis set, we have the expressions $|H\rangle = \frac{1}{\sqrt{2}}(|+\rangle + |-\rangle)$, $|V\rangle = \frac{i}{\sqrt{2}}(-|+\rangle + |-\rangle)$. Inserting these two expressions to $|\varphi_i\rangle$, the preselection could be rewritten as

$$|\psi_i\rangle = \frac{1-i}{\sqrt{2}}\left[\cos\left(\alpha - \frac{\pi}{4}\right)|+\rangle + \cos\left(\alpha + \frac{\pi}{4}\right)|-\rangle\right] \tag{Equation 26}$$

The second Glan laser polarizer (GLP2) is employed to achieve the postselection state $|V\rangle$, which can be written as:

$$|\psi_f\rangle = \frac{i}{\sqrt{2}}(|-\rangle - |+\rangle). \tag{Equation 27}$$

Finally, weak value can be obtained as:

$$A_w = \frac{\langle\varphi_f|\widehat{A}|\varphi_i\rangle}{\langle\varphi_f|\varphi_i\rangle} = \frac{\begin{bmatrix} \frac{-i}{\sqrt{2}} & \frac{i}{\sqrt{2}} \end{bmatrix} \times \begin{bmatrix} 1 & 0 \\ 0 & -1 \end{bmatrix} \times \begin{bmatrix} \frac{1-i}{2}(\cos\alpha + \sin\alpha) \\ \frac{1-i}{2}(\cos\alpha - \sin\alpha) \end{bmatrix}}{\begin{bmatrix} \frac{-i}{\sqrt{2}} & \frac{i}{\sqrt{2}} \end{bmatrix} \times \begin{bmatrix} \frac{1-i}{2}(\cos\alpha + \sin\alpha) \\ \frac{1-i}{2}(\cos\alpha - \sin\alpha) \end{bmatrix}} = \cot(\alpha) \tag{Equation 28}$$

Sample fabrication

The metasurface is fabricated by a femtosecond laser etching space-varying grooves at subwavelength scale. Under intense laser irradiation, the uniform glass (SiO_2) decomposes into porous glass ($SiO_{2(1-x)} + xO_2$). A periodic change of the laser intensity will lead to a modulation of the refractive index, because the laser intensity determines the refractive index (Ling et al., 2015). When the dimension of the structure is much smaller than the wavelength of the incident beam, only the zero-order diffraction mode can appear and the modes of other orders are suppressed. Thus, the function of metasurface is equivalent to spatially varying uniaxial crystals, with local optical axis (slow axis and fast axis) direction parallel or perpendicular to the direction of the groove, which presents a spatially varying effective birefringence. The birefringence phase retardation is given by

$$\Gamma = 2\pi(n_e - n_o)d/\lambda \tag{Equation 29}$$

where d indicates writing depth and $(n_e - n_o)$ is the induced birefringence. The ordinary and extraordinary refractive indices are

$$n_o = \sqrt{fn_1^2 + (1-f)n_2^2}, \tag{Equation 30}$$

$$n_e = \sqrt{\frac{n_1^2 n_2^2}{f n_2^2 + (1 - f) n_1^2}}$$

(Equation 31)

where f is the filling factor, and n_1, n_2 are the refractive indices of two media that constitute the nanograting. For the metasurface sample with π phase retardation at a wavelength of 632.8 nm, the filling factor is 0.1–0.2, with the line width of 30–50 nm and the writing period of 250–300 nm. The writing depth is about 80 μm and the value of n_e-n_o is about 3×10^{-3}. The microstructural region is located in the central part of the substrate plane, with 6 mm × 6 mm.

Sample preparation

The L-proline and D-proline samples are derived from the Aladdin company. In this system, the He-Ne laser with the central wavelength of 632.8 nm is from Thorlabs (HNL210LB), which has excellent beam quality and gas discharge laser characteristics. The CCD Camera Beam Profiler is from Thorlabs (CS165CU), which has flexible mounting options and compact size. This camera has a low <4.0 e^- read noise and high sensitivity while maintaining a small footprint. The global shutter captures the entire field of view simultaneously, allowing for imaging of rapidly changing scenes.

Experimental measurements

The temperature of chiral sample solution is about $12°C$ and the experimental environment is at room temperature $15°C$. After calculating the relationship between amplified beam shifts and preselected angles, we experimentally select chiral objects with different handedness and different concentrations, finally chiral edge images can be observed by our proposed scheme.